A wall model learned from the periodic hill data and the law of the wall ⊘

Zhou Zhideng (周志登) ⓘ ; Yang Xiang I. A. (杨翔) ⓘ ; Zhang Fengshun (张风顺) ⓘ ; Yang Xiaolei (杨晓雷) ✉ ⓘ

Check for updates

View Online   Export Citation

08 April 2024 03:26:35

Physics of Fluids

Special Topic:
Flow and Civil Structures

Submit Today

AIP Publishing

A wall model learned from the periodic hill data and the law of the wall

View Online   Export Citation   CrossMark

Zhideng Zhou (周志登),[1,2] [iD] Xiang I. A. Yang (杨翔),[3] [iD] Fengshun Zhang (张凤顺),[1,2] [iD] and Xiaolei Yang (杨晓雷)[1,2,a] [iD]

AFFILIATIONS

[1]The State Key Laboratory of Nonlinear Mechanics, Institute of Mechanics, Chinese Academy of Sciences, Beijing 100190, China
[2]School of Engineering Sciences, University of Chinese Academy of Sciences, Beijing 100049, China
[3]Department of Mechanical Engineering, Pennsylvania State University, State College, Pennsylvania 16802, USA

[a]Author to whom correspondence should be addressed: xyang@imech.ac.cn

ABSTRACT

Toward data-driven wall-modeled large-eddy simulations of different wall-bounded turbulent flows, a wall model is learned in this work using the wall-resolved large-eddy simulation (WRLES) data of the flow over periodic hills (PH) and the law of the wall (LoW). The feedforward neural network (FNN) is employed to construct the model. The obtained FNN_PH-LoW model is successfully tested using the direct numerical simulation data of turbulent channel flows and the WRLES data of PH cases, and applied to turbulent channel flows for a wide range of Reynolds numbers.

Published under an exclusive license by AIP Publishing. https://doi.org/10.1063/5.0143650

I. INTRODUCTION

Wall-modeled large-eddy simulation (WMLES) is promising for simulating industrial turbulent flows at a high Reynolds number.[1–5] A wall model, which can properly mimic the effect of the wall on the outer flow, is the key for the success of WMLES. The conventional wall models, which are often derived based on the equilibrium assumption, cannot accurately predict turbulent flows with separation. The machine learning method has become a powerful tool for different problems in fluid mechanics,[6,7] e.g., the development of turbulence models,[8–14] temporal prediction of turbulence,[15–18] reconstruction of the turbulent flow fields,[19–24] turbulence identification,[25–27] and turbulent flow control.[28–30] In our recent work,[31] we developed a wall model using the feedforward neural network (FNN) and the data of turbulent flow over periodic hills [which is dubbed as the FNN_periodic hills (FNN_PH) model in this paper]. With the aim that the data-trained model obeys the law of the wall for attached flows (e.g., fully developed turbulent channel flows and turbulent boundary layer flows), a new version of the FNN_PH model is trained to satisfy the law of the wall (dubbed as FNN_PH-LoW) and systematically tested using the cases with and without flow separation.

The development of wall models using the machine learning technique dates back to the work by Milano and Koumoutsakos,[32] in which the neural network was employed to construct the near wall flow in a turbulent channel flow. In the work by Yang *et al.*,[33] a wall model based on a physics-informed neural network was developed

and successfully applied to turbulent channel flows at various Reynolds numbers. A similar neural network was then employed to develop a wall model for spanwise rotating turbulent channel flows by Huang *et al.*[34] In the work by Bae and Koumoutsakos,[35] a wall model based on the reinforcement learning approach was developed and successfully applied to the turbulent channel flows at high Reynolds number. For turbulent flows with separation, Zhou *et al.*[31] developed a wall model based on neural networks and the data from the turbulent flow over periodic hills, with the successful *a priori* tests and *a posteriori* applications to turbulent channel flows. In the work by Zhou *et al.*,[36] the multi-agent reinforcement learning[35] was used to develop a wall model for the turbulent flow over periodic hills, which showed better predictions on the mean wall shear stress and velocity profiles than the equilibrium wall model at the trained Reynolds number. To develop a wall model for simulating different flow regimes, Lozano-Durán and Bae[37] proposed a methodology including a predictor and a classifier with the wall models trained using direct numerical simulation (DNS) data of several canonical turbulent flows. In the recent work by Lozano-Durán and Bae,[38] the model was further developed using the WMLES data for training to account for the error due to the discretization scheme and the grid employed in WMLES.

It is always the hope that the learned wall model is applicable to different wall-bounded turbulent flows. One basic requirement is that the learned wall model can reproduce the law of the wall. Bin *et al.*[39] recently proposed a progressive machine learning paradigm to respect

less complex models when training wall models for complex flows, and tested using the logarithmic layer, channel, boundary layer, and rotating channel examples. Toward the development a generalized wall model, this work is devoted to learn a wall model, which works for the separated flows, for which the data are employed for training, and satisfies the law of the wall in the meantime.

In the rest of the paper, the employed training data are presented in Sec. II. In Sec. III, the neural network for constructing the wall model is introduced. Then, the *a priori* tests and *a posteriori* applications of the model are shown in Sec. IV. At last, conclusions from this study are drawn in Sec. V.

II. DATA PREPARATION

In this section, we describe the employed data, which include the periodic hill data and the data generated using the logarithmic law of the wall, for training the FNN_PH-LoW model.

A. Periodic hill data

The employed periodic hill data are from wall-resolved large-eddy simulations (WRLESs), which were reported in our previous papers.[31,40] Figure 1 shows the schematic of geometry, mesh, and time-averaged velocity field for the turbulent flow over periodic hills. The virtual flow simulator (VFS-Wind)[41] code was employed to carry out the flow simulations, in which the governing equations are the three-dimensional unsteady spatially filtered incompressible Navier–Stokes equations in non-orthogonal, generalized curvilinear coordinates, shown as follows:

$$J \frac{\partial U^j}{\partial \xi^j} = 0,$$
$$\frac{1}{J}\frac{\partial U^i}{\partial t} = \frac{\xi_l^i}{J}\left(-\frac{\partial}{\partial \xi^j}(U^j u_l) - \frac{1}{\rho}\frac{\partial}{\partial \xi^j}\left(\frac{\xi_l^j p}{J}\right) + \frac{\mu}{\rho}\frac{\partial}{\partial \xi^j}\left(\frac{g^{jk}}{J}\frac{\partial u_l}{\partial \xi^k}\right) - \frac{1}{\rho}\frac{\partial \tau_{lj}}{\partial \xi^j} \right),$$

(1)

where x_i and ξ^i are the Cartesian and curvilinear coordinates, respectively, $\xi_l^i = \partial \xi^i / \partial x_l$ are the transformation metrics, J is the Jacobian of the geometric transformation, u_i is the ith component of the velocity vector in Cartesian coordinates, $U^i = (\xi_m^i / J) u_m$ is the contravariant volume flux, $g^{jk} = \xi_l^j \xi_l^k$ are the components of the contravariant metric tensor, and p is the pressure. In the momentum equation, τ_{ij}
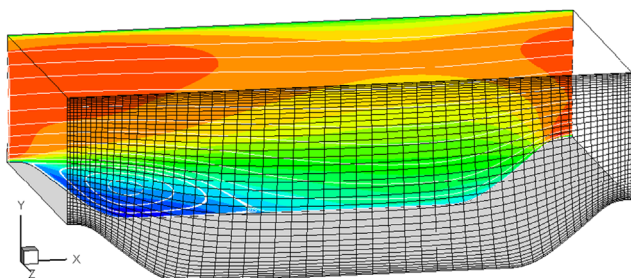

FIG. 1. Schematic of geometry, mesh, and time-averaged velocity field for the turbulent flow over periodic hills. The employed curvilinear mesh for WRLES is displayed every fifth grid line.

TABLE I. Parameters for the WRLES of turbulent flow over periodic hills, where α denotes the multiplicative factor for hill geometry[31,43] (the lower the α value, the steeper the hill, and $\alpha = 1.0$ denotes the baseline in Fig. 1) and Δy_c is the height of the first off-wall grid node.

Case	Re_h	Mesh $(N_x \times N_y \times N_z)$	α	Δt $(\times 10^{-2})$	$\Delta y_c/h$ $(\times 10^{-3})$
1 (Hill_B)	5600	$297 \times 193 \times 187$	1.0	1.0	1.5
2 (Hill_S)	10 595	$267 \times 193 \times 187$	0.5	1.0	1.5
3 (Hill_B)	10 595	$297 \times 193 \times 187$	1.0	1.0	1.5
4 (Hill_L)	10 595	$327 \times 193 \times 187$	1.5	1.0	1.5

represents the anisotropic part of the subgrid-scale stress tensor, which is modeled by the Smagorinsky model (SM)

$$\tau_{ij} - \frac{1}{3}\tau_{kk}\delta_{ij} = -2\nu_t \bar{S}_{ij},$$

(2)

where $\bar{S}_{ij} = \frac{1}{2}\left(\frac{\partial U_i}{\partial x_j} + \frac{\partial U_j}{\partial x_i}\right)$ is the filtered strain-rate tensor and ν_t is the eddy viscosity calculated by

$$\nu_t = (C_S \Delta)^2 |\bar{S}|,$$

(3)

where C_S is the model coefficient, and it is calculated dynamically using the dynamic Smagorinsky model (DSM) developed by Germano *et al.*,[42] $|\bar{S}| = \sqrt{2\bar{S}_{ij}\bar{S}_{ij}}$ and $\Delta = J^{-1/3}$ is the filter size, where J^{-1} is the cell volume.

The computational parameters of the WRLES cases employed in this work are listed in Table I. The data from cases 1 and 3 are employed for training the model, while the rest are employed for testing. For each case, nine snapshots per one flow-through time ($T = L_x/U_b$) on four spanwise ($x - y$) slices located at $z/h = 0.0$, 1.125, 2.25, and 3.375 are saved for a total simulation time $50T$. For each snapshot, the velocity and pressure gradient data at 95 nodes, which are uniformly distributed in $h_{wm}/h \in [0.006, 0.1]$ in the wall-normal direction, and the corresponding wall shear stress are extracted using the triangulation with linear interpolation approach. With the flow data, the input features and output labels as listed in Table II are computed for the neural network. The input features consist of the wall-normal distance h_{wm}, the three velocity components $u_{w,t}$, $u_{w,n}$, and u_s in the wall-tangential, wall-normal, and spanwise directions and the pressure gradients $\frac{\partial p}{\partial w_t}$, $\frac{\partial p}{\partial w_n}$ in the wall-tangential and wall-normal directions at three wall-normal points, with the distance between two adjacent points $\Delta h = 0.03h$. The wall-normal distance is normalized by a near-wall length scale $y^* = \nu/u_{\tau p}$,[44] where $u_{\tau p}$

$= \sqrt{u_v^2 + u_p^2}$, $u_v = \sqrt{|\frac{\nu u_{w,t}}{h_{wm}}|}$, $u_p = |\frac{\nu}{\rho}\frac{\partial p}{\partial w_t}|^{1/3}$. The output labels

TABLE II. The inputs and outputs for training the FNN model. The inputs are taken at three points in the wall-normal direction with the distance between two adjacent points $\Delta h = 0.03h$.

Input	Output
$\ln\left(\frac{h_{wm}}{y^*}\right)$, $\frac{u_{w,t}}{h_{wm}} \cdot \frac{\delta}{u_b}$, $\frac{u_{w,n}}{h_{wm}} \cdot \frac{\delta}{u_b}$, $\frac{u_s}{h_{wm}} \cdot \frac{\delta}{u_b}$, $\frac{\partial p}{\partial w_t} \cdot \frac{h_{wm}}{\delta}$, $\frac{\partial p}{\partial w_n} \cdot \frac{h_{wm}}{\delta} \cdot \frac{\delta}{u_b^2}$	$\frac{\tau_{w,t}}{u_b^2}$, $\frac{\tau_{w,s}}{u_b^2}$

consist of the wall-tangential and spanwise wall shear stresses. More details about the data preparation can be found in Ref. 31.

B. Data from the law of the wall

We employ a simple but general approach to incorporate the law of the wall (LoW) in the present wall model, that a certain amount of data are generated using the LoW. In this work, the logarithmic law for a smooth wall in the following form is employed:

$$U^+ = \frac{1}{\kappa} \ln(y^+) + B, \tag{4}$$

where the von Kármán constant $\kappa \approx 0.41$, $B = 5.2$, the normalized mean streamwise velocity $U^+ = U/u_\tau$, $y^+ = y u_\tau/\nu$, and the friction velocity $u_\tau = \sqrt{\tau_w/\rho}$ (τ_w is the wall shear stress, $\nu = \mu/\rho$ is the kinematic viscosity).

With the LoW, the training data are generated in the following four steps:

1. Sample $N_R = 701$ cases for $Re_\tau \in [10^2, 10^9]$ in the following way:

$$Re_\tau(m) = 10^{2 + \frac{7m}{N_R - 1}}, \quad m = 1, 2, \ldots, N_R - 1, \tag{5}$$

   where $Re_\tau = u_\tau \delta/\nu$ is the friction Reynolds number, δ is the characteristic length, e.g., boundary layer thickness.

2. For each Re_τ, sample the velocity and wall shear stress data using the LoW at the wall-normal locations in the range of $h_{wm} \in [\frac{30}{Re_\tau}, 0.1]$,

$$h_{wm} = 10^{\lg \frac{30}{Re_\tau} + j \cdot dh}, \tag{6}$$

   where j is the grid index in the wall-normal direction, and $dh = 0.002$ in this work.

3. Normalize the velocity and wall shear stress using the bulk velocity, which is calculated by integrating on the LoW in the range of $y^+ \in [0, Re_\tau]$ using the following empirical formula:

$$U_b = \int_0^{Re_\tau} \frac{U^+}{Re_\tau} dy^+ + 0.5. \tag{7}$$

   This is to ensure the obtained flow data are consistent with the present WMLES, in which the bulk velocity is employed for normalization.

4. Prepare the inputs and outputs listed in Table II. For the data from the LoW, the 3rd, 4th, 6th input and the 2nd output listed in Table II are set to zero. The 5th input is also zero in the original data. To prepare the data as the input for training and testing the model, normalization of the inputs is performed. During the normalization, the 5th input is allowed to change, while the 3rd, 4th, *and* 6th of the inputs are fixed at zero. This is based on the consideration that the learned model should be well posed as for the actual physical problem. Considering the law of wall, there are three independent variables to determine the friction velocity, i.e., the streamwise velocity, the corresponding wall-normal position, and the molecular viscosity.

III. CONSTRUCTION OF DATA-DRIVEN WALL MODEL

A feedforward neural network similar to that in our previous work,[31] which includes six hidden layers with 15 neurons in each layer,

is employed to construct the data-driven wall model. The activation function employed in this paper, which is the rectified linear unit (ReLU) in Ref. 31, is the hyperbolic tangent (tanh)[45] in the following form:

$$f(x) = \frac{e^x - e^{-x}}{e^x + e^{-x}}. \tag{8}$$

The prepared input and output data (denoted as x) are normalized using the Min–Max scaling

$$x^* = \frac{2(x - x_{\min})}{x_{\max} - x_{\min}} - 1. \tag{9}$$

The error backpropagation (BP) scheme[46] implemented with TensorFlow[47] is employed to train the FNN wall model. The key steps for training can be found in Sec. III A of Ref. 31. The procedure for calculating the output based on the input in the FNN, which includes the linear matrix manipulation of the weight and bias coefficients and the nonlinear mapping using the activation function, was shown in Appendix C of Ref. 31.

The number of input–output pairs from the LoW and PH case is both 1.1×10^6, of which 90% are used as training dataset and the rest 10% are employed for validation, and the batch size is 2×10^5. The loss function is defined as the weighted sum of mean square error (MSE) from the data of LoW (loss_1) and PH case (loss_2)

$$\begin{cases} \text{loss} = a_1 \cdot \text{loss\_1} + a_2 \cdot \text{loss\_2}, \\ \text{loss\_1} = \frac{1}{N_1} \sum_{i=1}^{N_1} (\mathbf{Y}_{1,i} - \mathbf{Y}_{1,i}{}^*)^2, \\ \text{loss\_2} = \frac{1}{N_2} \sum_{i=1}^{N_2} (\mathbf{Y}_{2,i} - \mathbf{Y}_{2,i}{}^*)^2, \end{cases} \tag{10}$$

where N_1 and N_2 are the number of training samples for LoW and PH case, and $\mathbf{Y}^*$ and $\mathbf{Y}$ denote the FNN output and labeled output, respectively. In this work, the weights of $a_1 = 1000$, $a_2 = 1$ are employed. This is due to the different convergence rates for training the model using the PH data and the LoW data. A higher weight for the loss of the LoW data is to make the contribution of loss function from the data of LoW and PH case comparable, so that both the complex flow characteristics in the PH case and the logarithmic law could be included in the trained model. Two models with $a_1 = 500$ and $a_2 = 1$, and $a_1 = 2000$ and $a_2 = 1$ were also trained and tested, showing that the model performance does not particularly depends on the choices of a_1 and a_2.

Figure 2 plots the variations of loss_1 and loss_2 with the training epochs. Initially, both the losses are large because the weight coefficients in the FNN are randomly set and the bias coefficients are set to zero. With the adjustment of the weight and bias coefficients, the loss_1 rapidly decreases as the functional form of LoW is easy to approximate, while the loss_2 decreases at a much lower rate because of the complicated flow field near the wall of the PH case and possibly the influence from the LoW data.

IV. EVALUATION OF THE FNN_PH-LOW WALL MODEL

The predictive capacity of the FNN_PH-LoW model is first evaluated using the DNS results of turbulent channel flows at $Re_\tau = 1000$ and 5200.[48] In this test, the FNN_PH-LoW model computes the wall
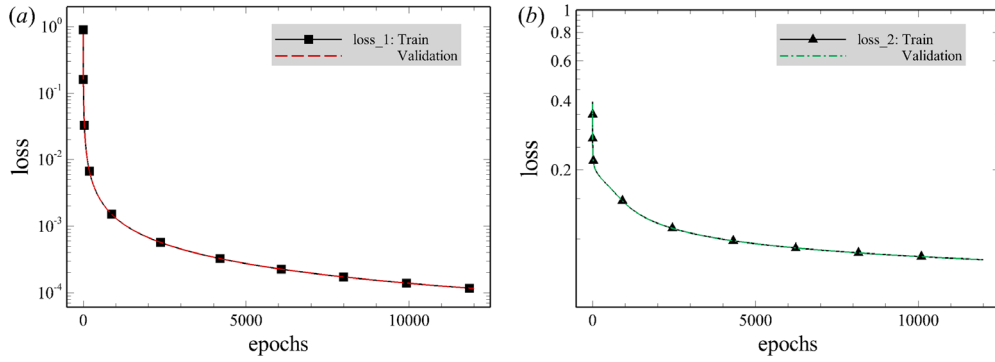
08 April 2024 03:26:35

FIG. 2. Variations of (a) loss_1 and (b) loss_2 with training epochs.

shear stress based on the mean streamwise velocity at different wall-normal positions. Figure 3 compares the predictions from the data-driven models with the DNS results. The y axis indicates the position of the first off-wall grid node of the three grid nodes employed as input features. The target values of wall shear stresses are $\tau_{w,t} = -1$, $\tau_{w,s} = 0$. Discrepancies are observed for the FNN_PH model[31] trained using only the PH case. After coupling the data

generated using the LoW, the FNN_PH-LoW model accurately predicts both the spanwise and streamwise wall shear stresses for the input data located at different wall-normal positions especially for $h_{wm}/\delta \in [0.003, 0.1]$.

The generalization capacity of the FNN_PH-LoW model is then tested using the PH data different from the training data, including different geometries (cases 2 and 4). Figures 4 and 5 depict the
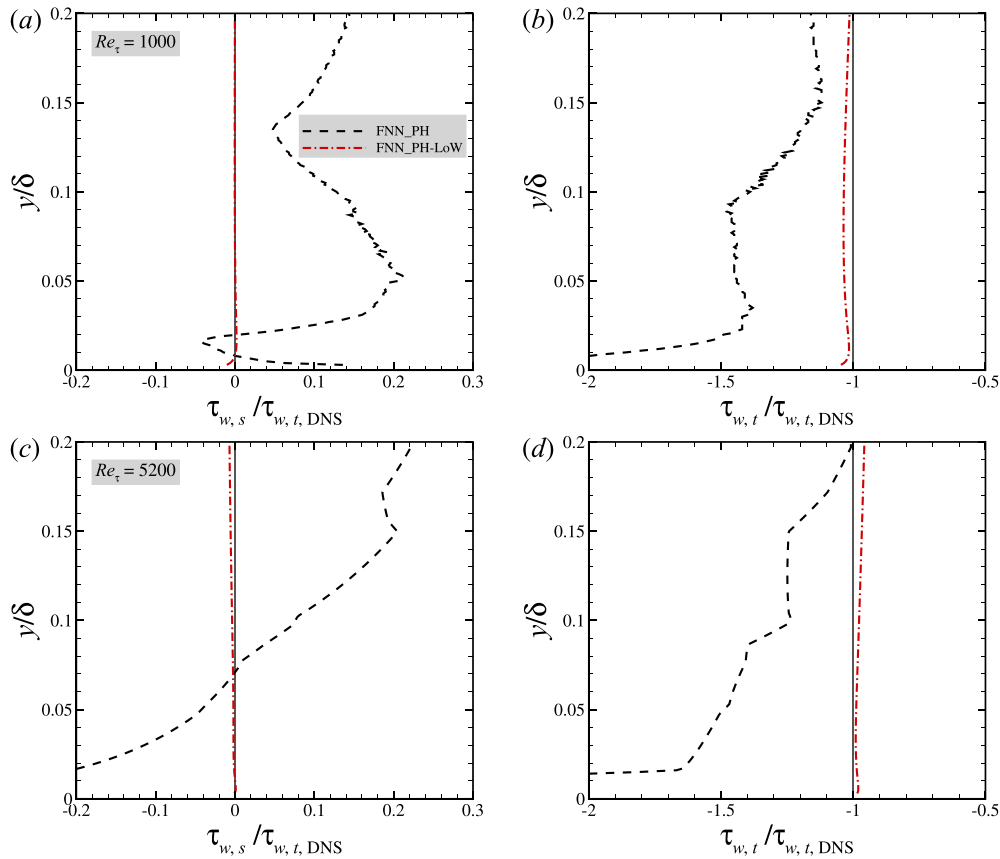

FIG. 3. Evaluation of the FNN_PH-LoW model using the DNS data of turbulent channel flows[48] for (a), (c) the spanwise component $\tau_{w,s}$ and (b), (d) the streamwise component $\tau_{w,t}$ of the wall shear stress. The predictions of the FNN_PH model[31] are also plotted for comparison.
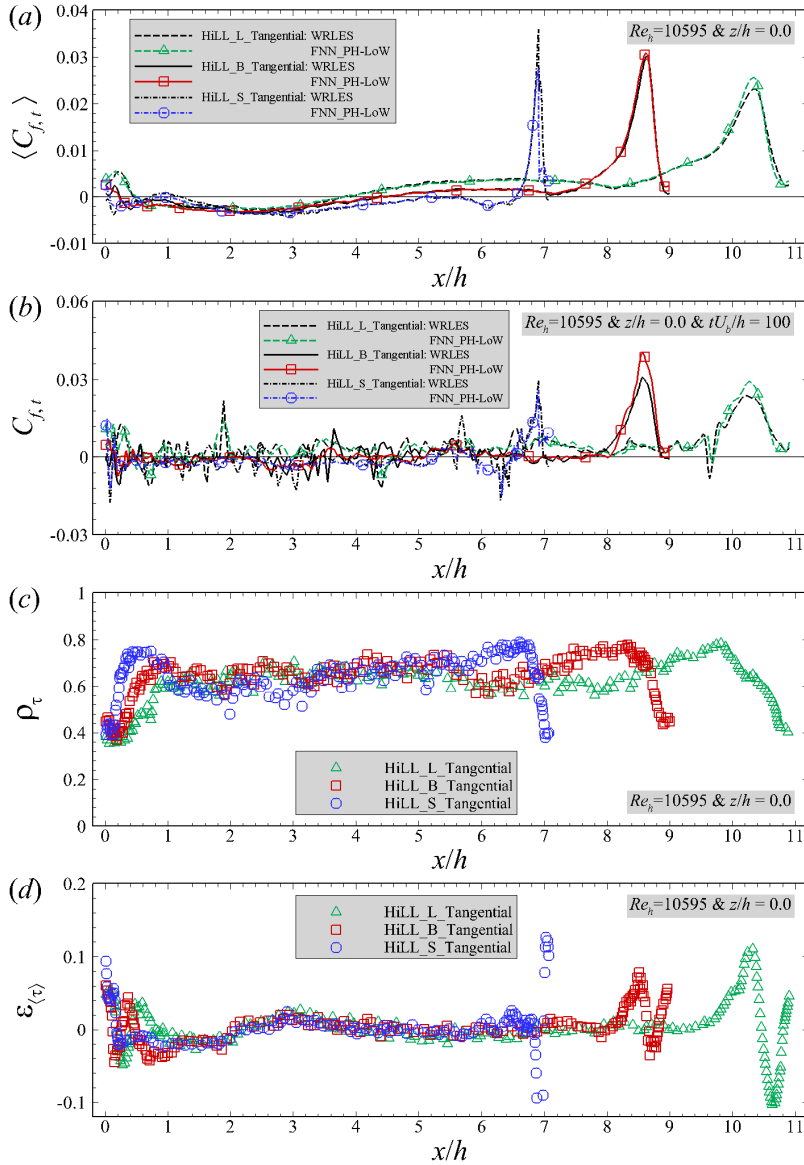
FIG. 4. Evaluation of the FNN_PH-LoW model in predicting the tangential wall shear stresses in the PH cases for (a), (b) the time-averaged and instantaneous tangential skin friction coefficients, (c) the correlation coefficients [Eq. (11)] of the fluctuating part of the wall shear stress, and (d) the relative error [Eq. (12)] of the time-averaged wall shear stress.

evaluation of the FNN_PH-LoW model on predicting the wall shear stresses, including the time-averaged and instantaneous value of wall-tangential and spanwise skin friction coefficients ($C_{f,t} = \tau_{w,t}/\frac{1}{2}\rho U_b^2$, $C_{f,s} = \tau_{w,s}/\frac{1}{2}\rho U_b^2$), the correlation coefficients (ρ_τ) of the fluctuating part of the wall shear stresses, and the relative error ($\varepsilon_{\langle\tau\rangle}$) of the time-averaged wall shear stresses, in which the ρ_τ and $\varepsilon_{\langle\tau\rangle}$ are defined as follows:

$$\rho_\tau = \frac{\langle(\tau_w^{\text{FNN}} - \langle\tau_w^{\text{FNN}}\rangle)\cdot(\tau_w^{\text{LES}} - \langle\tau_w^{\text{LES}}\rangle)\rangle}{\langle(\tau_w^{\text{FNN}} - \langle\tau_w^{\text{FNN}}\rangle)^2\rangle^{1/2}\langle(\tau_w^{\text{LES}} - \langle\tau_w^{\text{LES}}\rangle)^2\rangle^{1/2}}, \quad (11)$$

$$\varepsilon_{\langle\tau\rangle} = \frac{\langle\tau_w^{\text{FNN}}\rangle - \langle\tau_w^{\text{LES}}\rangle}{|\langle\tau_w^{\text{LES}}\rangle|_{\text{max}}}, \quad (12)$$

where "$\langle\ \rangle$" denotes the average over snapshots.

As seen in Figs. 4(a) and 4(b), the time-averaged and instantaneous tangential skin friction coefficients predicted by the FNN_PH-LoW model agree well with those from the WRLES for all three hill geometries, including some abrupt changes of $C_{f,t}$ observed at different streamwise positions. In Figs. 4(c) and 4(d), it is observed that the correlation coefficients are larger than 0.6 and the relative errors are smaller than 5% at most streamwise positions except for the locations near the crest of the hill, where the correlation coefficient is around 0.5, and the relative error is around 0.1. Compared with the results from the FNN_PH model (Figs. 8 and 12 in Ref. 31), the correlation coefficient is slightly decreased with similar relative error. As the model is not trained for any specific positions, that the flow is featured by sharply increases or decreases of force coefficients on the wall near the crest of the hill is the main reason for the relatively poor performance at corresponding locations.

As for the spanwise wall shear stress shown in Figs. 5(a) and 5(b), the time-averaged spanwise friction coefficients predicted by the FNN_PH-LoW model are around zero as expected. It is seen that the streamwise variations of the instantaneous spanwise friction coefficients are acceptable and captured by the FNN_PH-LoW model as well. The values of the correlation coefficients shown in Fig. 5(c) are observed being similar with those for the tangential wall shear stress.

At last, the *a posteriori* tests of the FNN_PH-LoW model are carried out by applying the model to WMLES of turbulent channel flows at different Reynolds numbers. The velocity and pressure gradient from WMLES are employed as the inputs to compute the wall shear stresses, which in turn are employed as the boundary condition for WMLES.

In the simulated cases, the dimensions of the channel are $7.0\delta \times 2.0\delta \times 3.5\delta$ in the streamwise, vertical, and spanwise directions, respectively, where δ is the half height of the channel. A wide range of bulk Reynolds numbers, i.e., $Re_b = U_b\delta/\nu = 19\,999 \sim 6.0 \times 10^9$, are considered. The channel is discretized using a grid of $64 \times 64 \times 64$, with the height of the first off-wall grid set to 0.03δ. To avoid the logarithmic layer mismatch,[49] the flow data starting from the second off-wall grid node at $h_{wm,1} = 0.045\delta$ and the following two grid nodes at $h_{wm,1} + 0.03\delta$ and $h_{wm,1} + 0.06\delta$ are employed as the inputs when using the FNN_PH-LoW model.

Figure 6 compares the mean streamwise velocity profiles from WMLES with the FNN_PH-LoW model and the LoW model, while the logarithmic law and the DNS data for $Re_\tau = 1000$ and 5200 (Refs. 48 and 50) are also plotted for comparison. For both wall models, a good agreement is observed for all the considered Reynolds numbers. In Figs. 7 and 8, the Reynolds stresses predicted by the WMLES are compared with the DNS results for $Re_\tau = 1000$ and 5200, respectively. The predictions from the FNN_PH-LoW model and the LoW model are close to each other. Compared with the DNS results, an overall good agreement is observed with discrepancies in the near-wall region, where the primary Reynolds shear stress and the vertical component of Reynolds normal stresses are underpredicted.

In addition to the wall model, the discretization scheme, the subgrid scale (SGS) model, and the quality of the employed grid also affect the predictive capability of WMLES. Here, the effects of the discretization scheme for the convection term and the SGS model are tested for WMLES of turbulent channel flows. Figure 9 plots the obtained mean streamwise velocity profiles. It is seen in Fig. 9(a) that the mean velocity profiles from the central difference scheme with the SM model ($C_S^2 = 0.01$) agree well with the DNS results and logarithmic law. The QUICK scheme, on the other hand, underpredicts the velocity at the first 2 to 3 off-wall grid nodes and shifts the velocity profile up in the logarithmic and wake
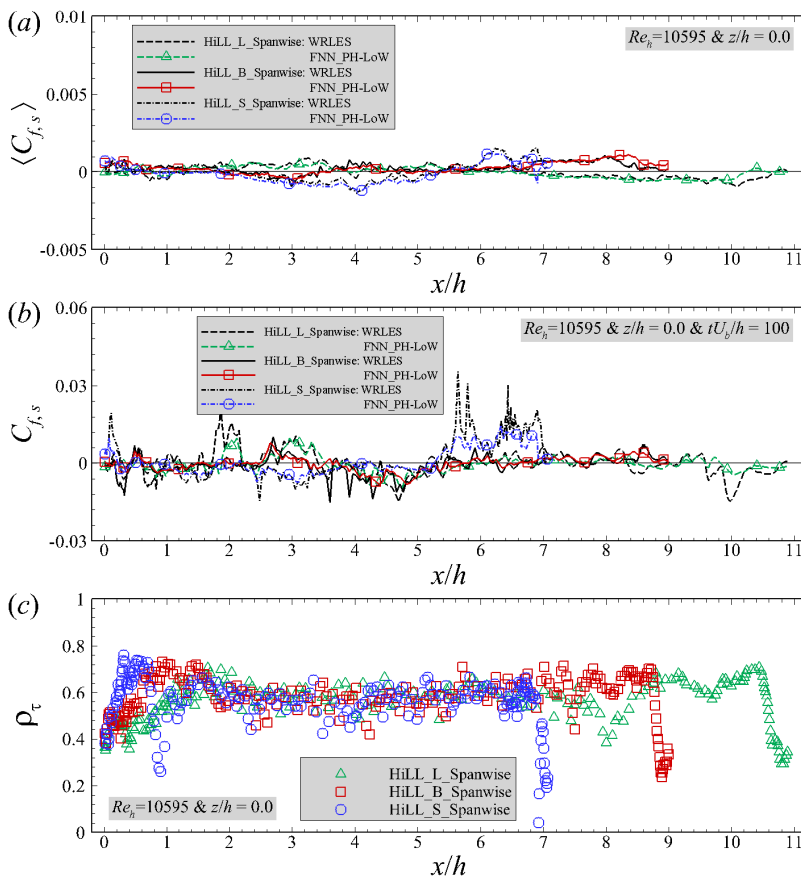

FIG. 5. Evaluation of the FNN_PH-LoW model in predicting the spanwise wall shear stresses in the PH cases for (a), (b) the time-averaged and instantaneous spanwise skin friction coefficients, and (c) the correlation coefficients [Eq. (11)] of the fluctuating part of the wall shear stress.
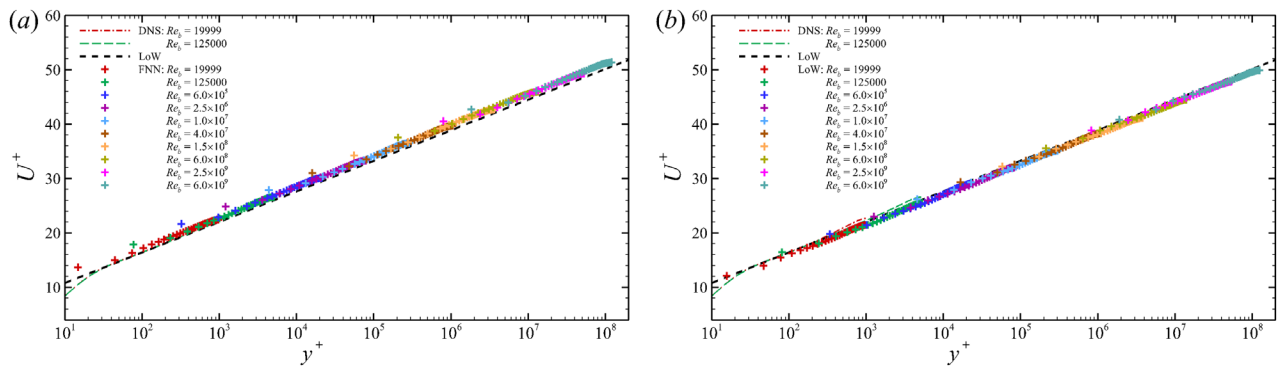
FIG. 6. Mean streamwise velocity profiles from the *a posteriori* tests of (a) the FNN_PH-LoW model and (b) the LoW model for turbulent channel flows at friction Reynolds numbers from $Re_b = 19\,999$ ($Re_\tau = 10^3$) to $Re_b = 6.0 \times 10^9$ ($Re_\tau = 1.2 \times 10^8$).

regions as shown in Fig. 9(b). When decreasing the coefficient to $C_S^2 = 0.001$, the velocity in the near-wall region (not the first 2 to 3 off-wall grid nodes) obeys the law of the wall (having the same slope), while deviates in the outer region by a larger slope and an upward shift as shown in Fig. 9(c). Figure 9(d) shows the results for $C_S^2 = 0.1$. As seen, the obtained mean velocity profiles are far from satisfactory that the large-eddy viscosity significantly decelerates the flow in the near-wall region.
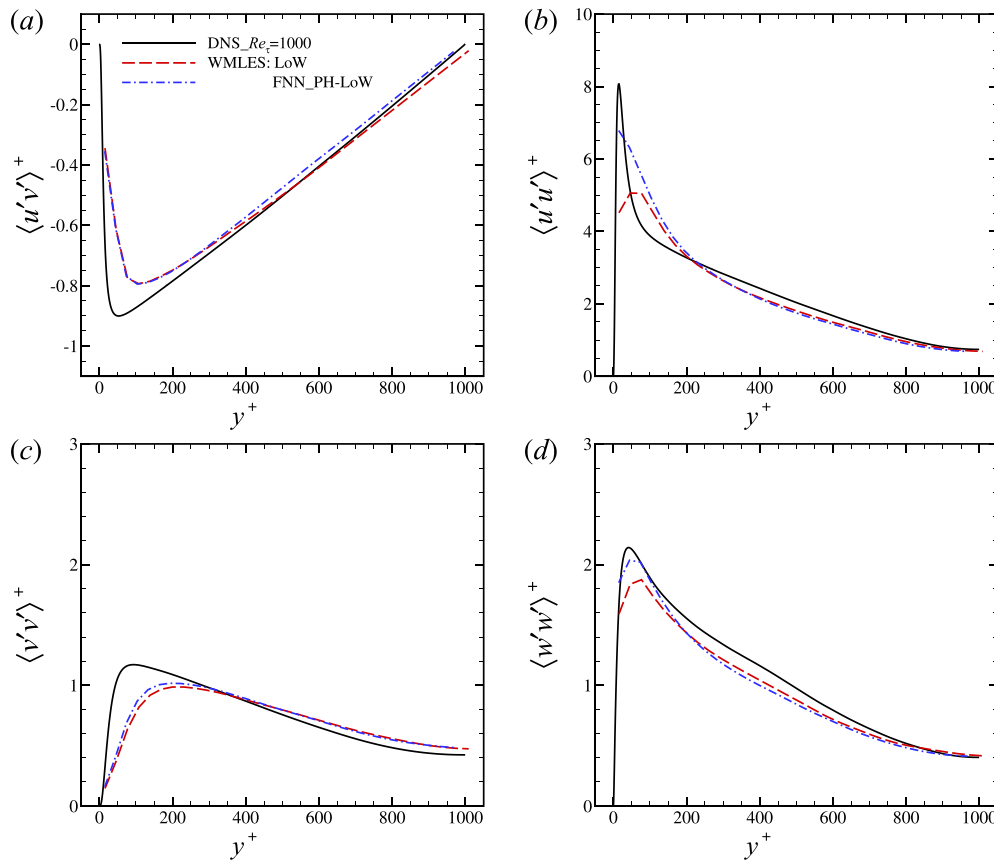

FIG. 7. Vertical profiles of (a) the primary Reynolds stress $\langle u'v' \rangle$, (b) the streamwise component $\langle u'u' \rangle$, (c) vertical component $\langle v'v' \rangle$, and (d) spanwise component $\langle w'w' \rangle$ of Reynolds normal stresses from the *a posteriori* tests of the FNN_PH-LoW model and the LoW model for turbulent channel flows at friction Reynolds number $Re_\tau = 1000$.
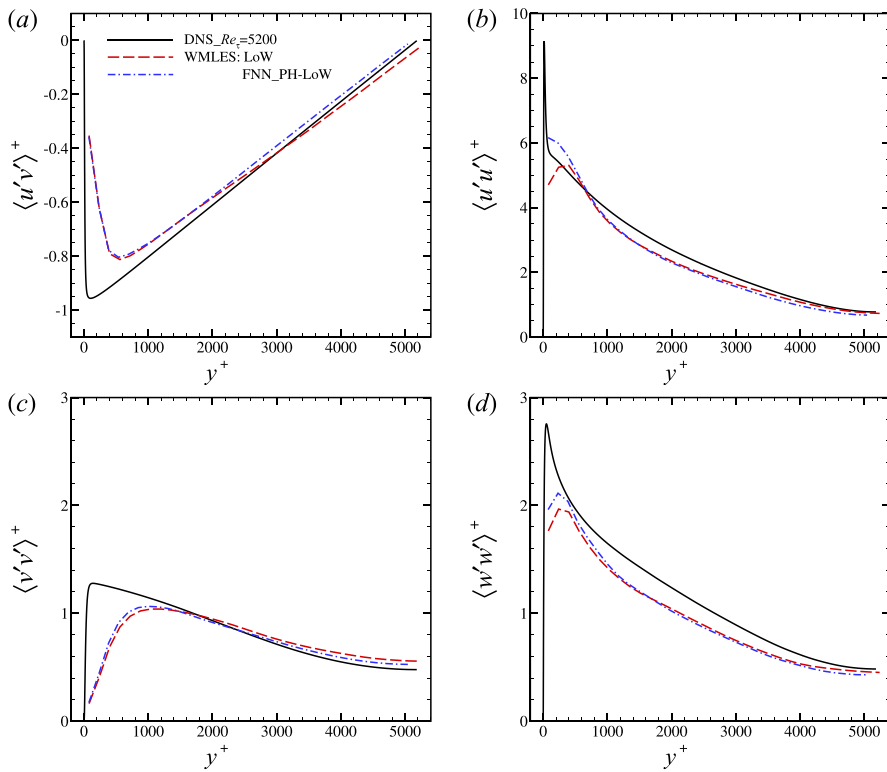
FIG. 8. Vertical profiles of (a) the primary Reynolds stress $\langle u'v' \rangle$, (b) the streamwise component $\langle u'u' \rangle$, (c) vertical component $\langle v'v' \rangle$, and (d) spanwise component $\langle w'w' \rangle$ of Reynolds normal stresses from the *a posteriori* tests of the FNN_PH-LoW model and the LoW model for turbulent channel flows at friction Reynolds number $Re_\tau = 5200$.
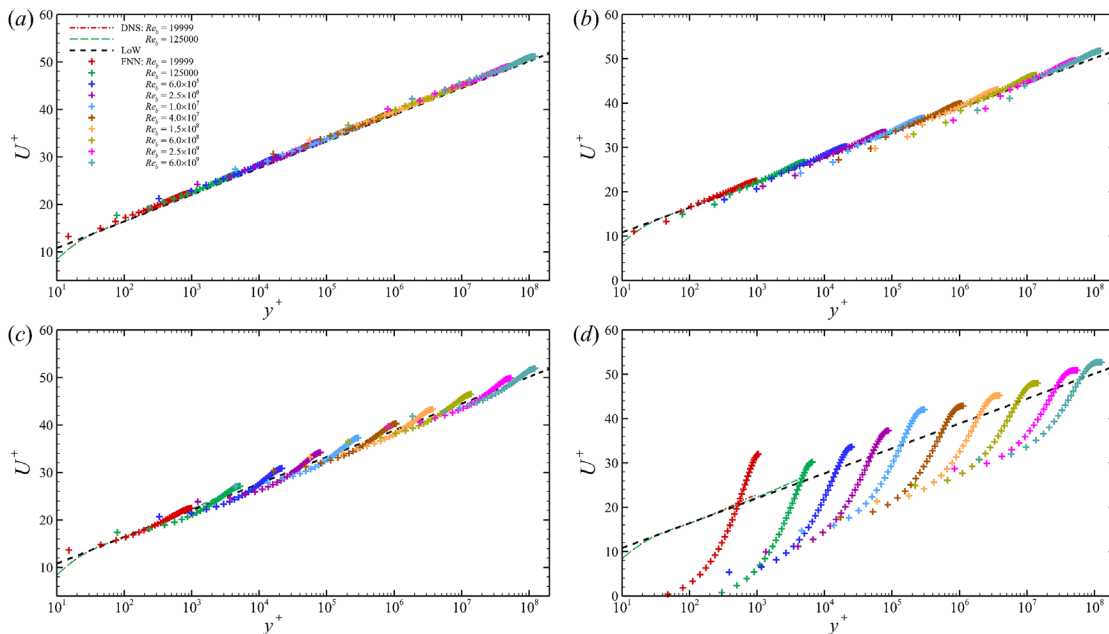

FIG. 9. Mean streamwise velocity profiles from the *a posteriori* tests of the FNN_PH-LoW model coupled with different discretization schemes for the convection term (a), (b) and different coefficients of the Smagorinsky model (c), (d): (a) central difference scheme and (b) QUICK scheme with $C_S^2 = 0.01$; (c) $C_S^2 = 0.001$ and (d) $C_S^2 = 0.1$ with the central difference scheme.

V. CONCLUSIONS

In this work, a data-driven wall model (dubbed as the FNN_PH-LoW model) was trained based on the WRLES data of the periodic hill cases and the law of the wall. To train the FNN wall model, the wall-normal distance, near-wall velocities, and pressure gradients as input features and the wall shear stresses as output labels are employed. In the *a priori* test, the trained wall model is evaluated using the DNS profiles of turbulent channel flows and the WRLES data of turbulent flow over periodic hills. In the *a posteriori* test, the WMLES cases of turbulent channel flows at a wide range of Reynolds numbers were carried out. In both *a priori* and *a posteriori* tests, an overall good performance was observed for the FNN_PH-LoW model.

It should be noted that combining the LoW data and PH data for model training is an approach employed to satisfy the LoW for the trained wall model. It is not intended to train a generalized wall model by mechanically adding new flow data, although combining several sets of typical flow data could be a feasible way to increase the generalizability of the learned wall model.

ACKNOWLEDGMENTS

AUTHOR DECLARATION

Conflict of Interest

The authors have no conflicts to disclose.

Author Contributions

Zhideng Zhou: Data curation (equal); Methodology (lead); Software (equal); Validation (lead); Visualization (lead); Writing – original draft (equal). **Xiang I. A. Yang:** Data curation (equal); Investigation (supporting); Supervision (supporting); Writing – review & editing (supporting). **Fengshun Zhang:** Data curation (supporting); Software (supporting); Validation (supporting). **Xiaolei Yang:** Conceptualization (lead); Funding acquisition (lead); Methodology (supporting); Supervision (equal); Writing – original draft (equal); Writing – review & editing (equal).

DATA AVAILABILITY

The data that support the findings of this study are available from the corresponding author upon reasonable request.

REFERENCES

[1]S. T. Bose and G. I. Park, "Wall-modeled large-eddy simulation for complex turbulent flows," Annu. Rev. Fluid Mech. **50**, 535–561 (2018).

[2]K. A. Goc, P. Moin, and S. T. Bose, "Wall-modeled large eddy simulation of an aircraft in landing configuration," AIAA Paper No. 2020-3002, 2020.

[3]X. L. Yang, C. Milliren, M. Kistner, C. Hogg, J. Marr, L. Shen, and F. Sotiropoulos, "High-fidelity simulations and field measurements for characterizing wind fields in a utility-scale wind farm," Appl. Energy **281**, 116115 (2021).

[4]X. I. A. Yang and K. P. Griffin, "Grid-point and time-step requirements for direct numerical simulation and large-eddy simulation," Phys. Fluids **33**, 015108 (2021).

[5]Z. D. Zhou, Z. B. Li, G. W. He, and X. L. Yang, "Towards multi-fidelity simulation of flows around an underwater vehicle with appendages and propeller," Theor. Appl. Mech. Lett. **12**, 100318 (2022).

[6]K. Duraisamy, G. Iaccarino, and H. Xiao, "Turbulence modeling in the age of data," Annu. Rev. Fluid Mech. **51**, 357–377 (2019).

[7]S. L. Brunton, B. R. Noack, and P. Koumoutsakos, "Machine learning for fluid mechanics," Annu. Rev. Fluid Mech. **52**, 477–508 (2020).

[8]J.-L. Wu, H. Xiao, and E. Paterson, "Physics-informed machine learning approach for augmenting turbulence models: A comprehensive framework," Phys. Rev. Fluids **3**, 074602 (2018).

[9]R. Maulik, O. San, A. Rasheed, and P. Vedula, "Data-driven deconvolution for large eddy simulations of Kraichnan turbulence," Phys. Fluids **30**, 125109 (2018).

[10]Z. D. Zhou, G. W. He, S. Z. Wang, and G. D. Jin, "Subgrid-scale model for large-eddy simulation of isotropic turbulent flows using an artificial neural network," Comput. Fluids **195**, 104319 (2019).

[11]C. Y. Xie, J. C. Wang, and E. Weinan, "Modeling subgrid-scale forces by spatial artificial neural networks in large eddy simulation of turbulence," Phys. Rev. Fluids **5**, 054606 (2020).

[12]X. W. Guo, Z. H. Xia, and S. Y. Chen, "Practical framework for data-driven RANS modeling with data augmentation," Acta Mech. Sin. **37**(12), 1748–1756 (2021).

[13]X.-L. Zhang, H. Xiao, X. D. Luo, and G. W. He, "Ensemble Kalman method for learning turbulence models from indirect observation data," J. Fluid Mech. **949**, A26 (2022).

[14]Z. Zhang, J. Z. Wang, R. F. Huang, R. D. Qiu, X. S. Chu, S. R. Ye, Y. W. Wang, and Q. K. Liu, "Data-driven turbulence model for unsteady cavitating flow," Phys. Fluids **35**, 015134 (2023).

[15]R. King, O. Hennigh, A. Mohan, and M. Chertkov, "From deep to physics-informed learning of turbulence: Diagnostics," arXiv:1810.07785v2 (2018).

[16]S. Lee and D. You, "Data-driven prediction of unsteady flow over a circular cylinder using deep learning," J. Fluid Mech. **879**, 217–254 (2019).

[17]T. Nakamura, K. Fukami, K. Hasegawa, Y. Nabae, and K. Fukagata, "Convolutional neural network and long short-term memory based reduced order surrogate for minimal turbulent channel flow," Phys. Fluids **33**, 025116 (2021).

[18]X. Y. Qu, Z. J. Liu, W. An, X. J. Liu, and H. Q. Lyu, "Dynamics-disentangled deep learning model for multi-cycle prediction of unsteady flow field," Phys. Fluids **34**, 095128 (2022).

[19]B. Liu, J. P. Tang, H. B. Huang, and X. Y. Lu, "Deep learning methods for super-resolution reconstruction of turbulent flows," Phys. Fluids **32**, 025105 (2020).

[20]F. Fukami, K. Fukagata, and K. Taira, "Machine-learning-based spatio-temporal super resolution reconstruction of turbulent flows," J. Fluid Mech. **909**, A9 (2021).

[21]H. P. Wang, Y. Liu, and S. Z. Wang, "Dense velocity reconstruction from particle image velocimetry/particle tracking velocimetry using a physics-informed neural network," Phys. Fluids **34**, 017116 (2022).

[22]Z. D. Zhou, B. L. Li, X. L. Yang, and Z. X. Yang, "A robust super-resolution reconstruction model of turbulent flow data based on deep learning," Comput. Fluids **239**, 105382 (2022).

[23]S. J. Laima, X. X. Zhou, X. W. Jin, D. L. Gao, and H. Li, "DeepTRNet: Time-resolved reconstruction of flow around a circular cylinder via spatiotemporal deep neural networks," Phys. Fluids **35**, 015118 (2023).

[24]R. Arun, H. J. Bae, and B. J. McKeon, "Towards real-time reconstruction of velocity fluctuations in turbulent channel flow," arXiv:2301.06734v1 (2023).

[25]Z. Wu, J. Lee, C. Meneveau, and T. Zaki, "Application of a self-organizing map to identify the turbulent-boundary-layer interface in a transitional flow," Phys. Rev. Fluids **4**, 023902 (2019).

[26]B. L. Li, Z. X. Yang, X. Zhang, G. W. He, B.-Q. Deng, and L. Shen, "Using machine learning to detect the turbulent region in flow past a circular cylinder," J. Fluid Mech. **905**, A10 (2020).

[27]K. Fukami, T. Murata, K. Zhang, and K. Fukagata, "Sparse identification of nonlinear dynamics with low-dimensionalized flow representations," J. Fluid Mech. **926**, A10 (2021).

[28]J. Park and H. Choi, "Machine-learning-based feedback control for drag reduction in a turbulent channel flow," J. Fluid Mech. **904**, A24 (2020).

[29]Y. Zhou, D. W. Fan, B. F. Zhang, R. Y. Li, and B. R. Noack, "Artificial intelligence control of a turbulent jet," J. Fluid Mech. **897**, A27 (2020).

[30]F. Ren, J. Rabault, and H. Tang, "Applying deep reinforcement learning to active flow control in weakly turbulent conditions," Phys. Fluids **33**, 037121 (2021).

[31]Z. D. Zhou, G. W. He, and X. L. Yang, "Wall model based on neural networks for LES of turbulent flows over periodic hills," Phys. Rev. Fluids **6**, 054610 (2021).

[32]M. Milano and P. Koumoutsakos, "Neural network modeling for near wall turbulent flow," J. Comput. Phys. **182**, 1–26 (2002).

[33]X. I. A. Yang, S. Zafar, J.-X. Wang, and H. Xiao, "Predictive large-eddy-simulation wall modeling via physics-informed neural networks," Phys. Rev. Fluids **4**, 034602 (2019).

[34]X. L. D. Huang, X. I. A. Yang, and R. F. Kunz, "Wall-modeled large-eddy simulations of spanwise rotating turbulent channels-Comparing a physics-based approach and a data-based approach," Phys. Fluids **31**, 125105 (2019).

[35]H. J. Bae and P. Koumoutsakos, "Scientific multi-agent reinforcement learning for wall-models of turbulent flows," Nat. Commun. **13**, 1443 (2022).

[36]D. Zhou, M. P. Whitmore, K. P. Griffin, and H. J. Bae, "Multi-agent reinforcement learning for wall modeling in LES of flow over periodic hills," arXiv:2211.16427v1 (2022).

[37]A. Lozano-Durán and H. J. Bae, "Self-critical machine-learning wall-modeled LES for external aerodynamics," arXiv:2012.10005v1 (2020).

[38]A. Lozano-Durán and H. J. Bae, "Building-block-flow wall model for large-eddy simulation," arXiv:2211.07879v1 (2022).

[39]Y. W. Bin, L. H. Chen, G. Huang, and X. I. A. Yang, "Progressive, extrapolative machine learning for near-wall turbulence modeling," Phys. Rev. Fluids **7**, 084610 (2022).

[40]Z. D. Zhou, T. Wu, and X. L. Yang, "Reynolds number effect on statistics of turbulent flows over periodic hills," Phys. Fluids **33**, 105124 (2021).

[41]X. L. Yang, F. Sotiropoulos, R. J. Conzemius, J. N. Wachtler, and M. B. Strong, "Large-eddy simulation of turbulent flow past wind turbines/farms: The virtual wind simulator (VWiS)," Wind Energy **18**(12), 2025–2045 (2015).

[42]M. Germano, U. Piomelli, P. Moin, and W. H. Cabot, "A dynamic subgrid-scale eddy viscosity model," Phys. Fluids A **3**, 1760 (1991).

[43]H. Xiao, J.-L. Wu, S. Laizet, and L. Duan, "Flows over periodic hills of parameterized geometries: A dataset for data-driven turbulence modeling from direct simulations," Comput. Fluids **200**, 104431 (2020).

[44]C. Duprat, G. Balarac, O. Métais, P. M. Congedo, and O. Brugière, "A wall-layer model for large-eddy simulations of turbulent flows with/out pressure gradient," Phys. Fluids **23**, 015101 (2011).

[45]I. Goodfellow, Y. Bengio, and A. Courville, *Deep Learning* (MIT Press, Cambridge, MA, 2016).

[46]D. E. Rumelhart, G. E. Hinton, and R. J. Williams, "Learning representations by back-propagating errors," Nature **323**, 533–536 (1986).

[47]M. Abadi, P. Barham, J. Chen, Z. Chen, A. Davis, J. Dean, M. Devin, S. Ghemawat, G. Irving, M. Isard *et al.*, "TensorFlow: A system for large-scale machine learning," in *Proceedings of the 12th USENIX Symposium on Operating Systems Design and Implementation* (USENIX Association, 2016), Vol. 16, pp. 265–283.

[48]See http://turbulence.pha.jhu.edu for J. Hopkins turbulence databases.

[49]X. I. A. Yang, G. I. Park, and P. Moin, "Log-layer mismatch and modeling of the fluctuating wall stress in wall-modeled large-eddy simulations," Phys. Rev. Fluids **2**, 104601 (2017).

[50]M. Lee and R. D. Moser, "Direct numerical simulation of turbulent channel flow up to $Re_\tau \approx 5200$," J. Fluid Mech. **774**, 395–415 (2015).